A space-time Bayesian hierarchical modeling framework for projection of seasonal maximum streamflow

Álvaro Ossandón[1,2], Manuela I Brunner[3,4], Balaji Rajagopalan[1,5], and William Kleiber[6]

[1]Department of Civil, Environmental and Architectural Engineering, University of Colorado, Boulder CO, USA
[2]Departamento de Obras Civiles, Universidad Técnica Federico Santa María, Valparaíso, Chile
[3]Research Applications Laboratory, National Center for Atmospheric Research, Boulder CO, USA
[4]Institute of Earth and Environmental Sciences, University of Freiburg, Freiburg, Germany
[5]Cooperative Institute for Research in Environmental Sciences, University of Colorado, Boulder CO, USA
[6]Department of Applied Mathematics, University of Colorado, Boulder CO, USA

Correspondence: Álvaro Ossandón (alvaro.ossandon@colorado.edu)

Abstract. Timely projections of seasonal streamflow extremes can be useful for the early implementation of annual flood risk adaptation strategies. However, predicting seasonal extremes is challenging particularly under nonstationary conditions and if extremes are correlated in space. The goal of this study is to implement a space-time model for the projection of seasonal streamflow extremes that considers the nonstationarity (inter-annual variability) and spatio-temporal dependence of high flows. We develop a space-time model to project seasonal streamflow extremes for several lead times up to 2 months using a Bayesian Hierarchical modeling (BHM) framework. This model is based on the assumption that streamflow extremes (3-day maxima) at a set of gauge locations are realizations of a Gaussian elliptical copula and generalized extreme value (GEV) margins with nonstationary parameters. These parameters are modeled as a linear function of suitable covariates describing the previous season selected using the deviance information criterion (DIC). Finally, the copula is used to generate streamflow ensembles, which capture spatio-temporal variability and uncertainty. We apply this modeling framework to predict 3-day maximum streamflow in spring (May-June) at seven gauges in the Upper Colorado River Basin (UCRB) with 0 to 2 months lead time. In this basin, almost all extremes that cause severe flooding occur in spring as a result of snowmelt and precipitation. Therefore, we use regional mean snow water equivalent and temperature from the preceding winter season as well as indices of large-scale climate teleconnections – ENSO, AMO, and PDO – as potential covariates for 3-day spring maximum streamflow. Our model evaluation, which is based on the comparison of different model versions and the energy skill score, indicates that the model can capture the space-time variability of extreme streamflow well and that model skill increases with decreasing lead time. We also find that the use of climate variables slightly enhances skill relative to using only snow information. Median projections and their uncertainties are consistent with observations thanks to the representation of spatial dependencies through covariates in the margins and a Gaussian copula. This spatio-temporal modeling framework helps to plan seasonal adaptation and preparedness measures as predictions of extreme spring streamflows become available 2 months before actual flood occurrence.

1 Introduction

Floods are a concern in mountain regions such as the Upper Colorado River Basin (UCRB), where streamflow extremes happen in spring due to snowmelt in combination with precipitation (McCabe et al., 2007), and are projected to increase under future climate conditions (Musselman et al., 2018). To reduce the negative impacts of such extreme events, we need tools that decision-makers can use in the mid - and long-term planning of flood risk adaptation strategies. Most existing tools either use hydrological models to provide operational daily forecasts at lead times ranging from 1 day to a couple of weeks or statistical models considering hydro-climatic variables from the previous season to generate seasonal streamflow forecasts. Both types of tools are useful to inform reservoir operations during the dry season or to provide high flow alerts at a local scale. However, they don't usually consider spatial dependencies in high flow occurrence in different catchments which is crucial to reliably estimate regional flood hazard (Brunner et al., 2020).

Operational streamflow forecasts are generally implemented using physically-based models that use forecasts of hydro-meteorological variables such as rainfall as their forcing (Clark and Hay, 2004; Ghile and Schulze, 2010; Wijayarathne and Coulibaly, 2020). An alternative to such physically based models are hybrid models which combine physically-based models with statistical models to post-process their output and to increase forecast skill (Chen et al., 2015; Kurian et al., 2020). Both types of models provide daily streamflow forecasts for short lead times (no longer than one or two weeks), may neglect spatial dependencies of flows in different catchments, and are deterministic or provide probabilistic ensemble forecasts by considering forcing perturbations (of precipitation and temperature), i.e. they don't usually depict model parameter uncertainty.

Only a few studies have tried to implement seasonal peak flow forecasts, e.g., Werner and Yeager (2013) generated both long- and short- leadtime forecasts during the 2011 runoff season at more than 400 locations in the Colorado River basin using two physically-based models. However, peak flow forecasts were skillful only after May 15th mainly because of inaccurate weather and climate forecasts. In addition, Kwon et al. (2009) generated annual maximum streamflow forecasts for the Three Gorges Dam in the Yangtze River basin in China considering sea surface temperature (SST) anomalies and snow cover from the previous season as covariates. However, these forecasts provided return level forecasts for single sites as they focused on reservoir operation.

Seasonal and sub-seasonal streamflow forecasting models rely on the skill of hydro-climatic variables from the previous season, such as snow cover (e.g., Kwon et al., 2009; Pagano et al., 2009; Livneh and Badger, 2020), large scale climate indices (Ruiz et al., 2007; Lima and Lall, 2010; Robertson and Wang, 2012), or changes in land cover conditions (Penn et al., 2020) among others to obtain skillful forecasts. Modeling approaches include statistical approaches based on multiple linear regression (Ruiz et al., 2007; Pagano et al., 2009; Penn et al., 2020); physically-based models that consider the uncertainty of initial conditions or inputs by perturbing them (Werner and Yeager, 2013; Anghileri et al., 2016; Wood et al., 2016); and Bayesian approaches that account for parameter uncertainty (Kwon et al., 2009; Lima and Lall, 2010; Robertson and Wang, 2012).

In the case of mountain regions, projection models for spring flow extremes can take advantage of the fact that snow water equivalents (SWE) accumulated until the beginning of spring are a skillful predictor of spring streamflow (Koster et al., 2010;

Livneh and Badger, 2020). However, such models should also consider potential nonstationarities (inter-annual-variability) due to climate change (Musselman et al., 2018) and the spatio-temporal dependence of the data as flood risk may increase if multiple catchments are affected at once (Thieken et al., 2015; Hochrainer-Stigler, 2020). Here, we develop a Bayesian Hierarchical Model (BHM) for the prediction of extreme spring streamflow that considers both nonstationarity and spatio-temporal dependence and ask:

- How does the representation of nonstationarity (inter-annual-variability) through suitable covariates improve seasonal predictions?

- How does the explicit representation of spatial dependencies improve prediction performance?

- To what extent are seasonal projections for longer lead times still skillful?

We address these questions by applying the proposed BHM to project 3-day spring maximum (May-June) streamflow at seven gauges in the Upper Colorado River Basin (UCRB). We consider 3-day maxima instead of 1-day maxima because snowmelt-driven events in spring typically have longer durations and flood volumes than events driven by convective storms in summer.

2 Proposed framework

We propose a space-time modeling framework for the prediction of seasonal streamflow extremes that has three components: (i) a hierarchical model structure, (ii) nonstationary margins, and (iii) a spatial dependence model. Each of these model components, their estimation strategies, and the estimation of ensembles of seasonal streamflow extremes are described below.

2.1 Hierarchical model structure

We conduct a nonstationary frequency analysis of seasonal streamflow extremes at m gauges in a river basin - say, $q_1, \ldots, q_m$ - over k years. To do this analysis, we consider a Bayesian hierarchical model that accounts for spatial dependence and nonstationarity. In the first layer of the hierarchical model structure, also known as the data layer, we consider that the joint distribution of streamflow at multiple gauges in each year is modeled using a Gaussian elliptical copula with generalized extreme value (GEV) margins (Coles, 2001; Katz, 2013; He et al., 2015). Specifically, the proposed model structure for m locations is

$$(q_1(t), \ldots, q_m(t)) \sim C_m\left(\boldsymbol{\Sigma}; \boldsymbol{\mu}(t), \boldsymbol{\sigma}(t), \boldsymbol{\xi}\right) \tag{1}$$

$$q_i(t) \sim GEV\left(\mu_i(t), \sigma_i(t), \xi_i\right), \quad i = 1, \ldots, m \tag{2}$$

where C_m is an m-dimensional Gaussian elliptical copula with dependence matrix $\boldsymbol{\Sigma}$ and GEV parameters (location, scale, and shape) $\mu_i(t) \in (-\infty, \infty)$, $\sigma_i(t) > 0$ and $\xi_i \in (-\infty, \infty)$. The second layer of the hierarchy, also known as the latent layer,
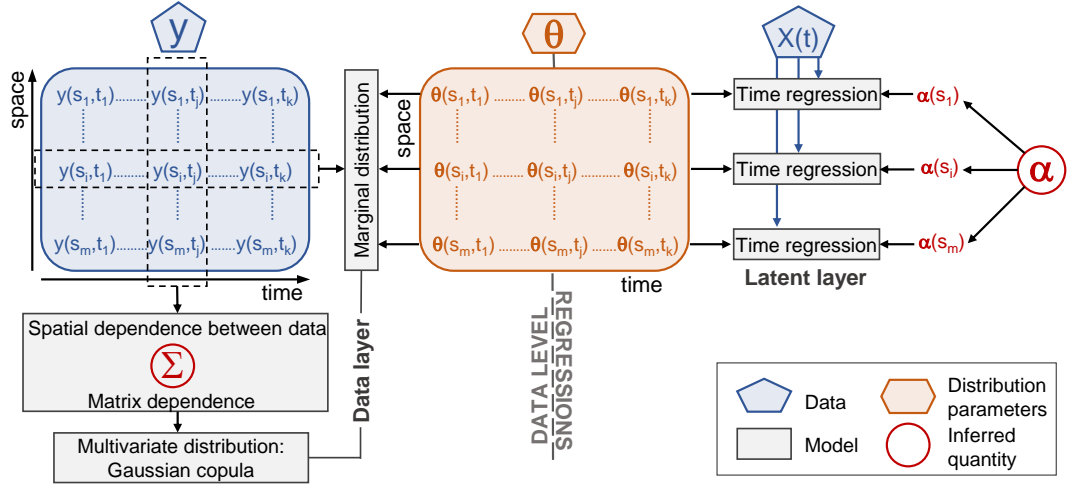
Figure 1. Conceptual sketch of the Bayesian Hierarchical Model. Blue boxes denote the data, orange boxes the GEV distribution parameters, grey boxes the models, and red circles the inferred quantities. Model boxes correspond to the data layer (Gaussian copula and GEV marginal distributions) and the latent layer (time regressions of GEV parameters). $\boldsymbol{\theta}\left(s_i, t_j\right) = \left[\boldsymbol{\mu}\left(s_i, t_j\right), \log \boldsymbol{\sigma}\left(s_i, t_j\right), \boldsymbol{\xi}\left(s_i, t_j\right)\right]$.

considers that the three parameters of the GEV are nonstationary and are time-varying, i.e., for the streamflow gauge i at time t, $\boldsymbol{\mu}\left(t\right) = \left[\mu_i\left(t\right)\right]_{i=1}^m$, $\boldsymbol{\sigma}\left(t\right) = \left[\sigma_i\left(t\right)\right]_{i=1}^m$, $\boldsymbol{\xi} = \left[\xi_i\right]_{i=1}^m$. Specifics of models (1) and (2) are given in the next sections.

A conceptual sketch of the BHM is shown in Fig. 1 which shows the data layer (Gaussian copula and GEV marginal distributions) and the latent layer (time dependence of GEV parameters).

2.2 Marginal distributions

The first two GEV parameters (location and scale) are modeled as linear functions of time-dependent large-scale climate variables and regional mean variables from the previous season while the shape parameter is considered to be stationary:

$$\mu_i\left(t\right) = \alpha_{\mu 0_i} + \sum_{j=1}^{n} \alpha_{\mu j_i} x_j\left(t\right), \quad i = 1, \ldots, m \tag{3}$$

$$\log\left(\sigma_i\left(t\right)\right) = \alpha_{\sigma 0_i} + \sum_{j=1}^{n} \alpha_{\sigma j_i} x_j\left(t\right), \quad i = 1, \ldots, m \tag{4}$$

$$\xi_i = \alpha_{\xi 0_i}, \quad i = 1, \ldots, m \tag{5}$$

where $x_j\left(t\right)$ is covariate j at time t, $\alpha_{\mu j_i}$, $\alpha_{\sigma j_i}$, and $\alpha_{\xi 0_i}$ are the regression coefficients for covariate j and gauge i at time t. $\log\left(\sigma\right)$ is used to ensure positive scale parameters. The validity of the nonstationary location and scale parameters can be checked through the significance of their slope coefficients' posterior PDFs (i.e., by checking whether 95% of the sample

95   values are greater (lower) than 0). Covariates will be discussed in section 3.2. The shape parameter ξ is often modeled as a single value per study area/region because of large estimation uncertainties (Cooley et al., 2007; Renard, 2011; Apputhurai and Stephenson, 2013; Atyeo and Walshaw, 2012) or modelled spatially along with the other GEV parameters but considering a specific range of potential values (Cooley and Sain, 2010; Bracken et al., 2016). Here, we model the shape parameter for each catchment individually but consider it to be stationary in time.

2.3   Gaussian copula for spatial dependence

100

Copulas are a flexible tool for modeling multivariate random variables since they can represent dependence independently of the choice of marginal distributions (Genest and Favre, 2007; Bracken et al., 2018; Brunner et al., 2019), which is a particularly appealing feature for extremal processes. This study focuses on Gaussian copulas because of their ease of implementation in a Bayesian and high-dimensional framework.

105   Let $\boldsymbol{q}(t) = [q_i(t)]_{i=1}^m$ be a random vector of extreme streamflow at m gauges and time t. The Gaussian copula builds the joint cumulative distribution function (CDF) of $\boldsymbol{q}(t)$ as

$$F_{cop}(\boldsymbol{q}(t)) = \Phi_\Sigma(\boldsymbol{u}(t)) \tag{6}$$

where $\Phi_\Sigma(\cdot)$ is the joint CDF of an m-dimensional multivariate normal distribution with dependence matrix Σ, $u(t) = [u_i(t)]_{i=1}^m$, $u_i(t) = \Phi^{-1}(F_{it}[q_i(t)])$ with Φ being the CDF of the standard normal distribution, and $F_{it}(\cdot)$ the marginal GEV

110   or empirical CDF for streamflow gauge i at time t.

    The copula dependence matrix, Σ, is a symmetric positive definite matrix that captures the strength of dependence between all gauge pairs using the Pearson correlation coefficient. The element c_{ij} of Σ quantifies the dependence between gauges i and j and its values can vary between -1 and 1:

$$\Sigma = \begin{bmatrix} 1 & c_{12} & \cdots & c_{1(m-1)} & c_{1m} \\ c_{21} & 1 & \ddots & \vdots & c_{2m} \\ c_{31} & c_{32} & \ddots & \vdots & \vdots \\ \vdots & \vdots & \ddots & 1 & c_{(m-1)m} \\ c_{m1} & c_{m2} & \cdots & c_{(m-1)m} & 1 \end{bmatrix} \tag{7}$$

115   By definition, the dependency between a streamflow gauge and itself is unity, so the diagonal elements of Σ are 1's. Since Σ is symmetric, only $m(m-1)/2$ values need to be fitted (values in the lower or upper triangle of Σ). The Gaussian copula only assumes linear correlation after quantile transformation of the marginals with the inverse normal CDF. This does not impose a linear correlation structure on the marginal distributions, meaning that nonlinear dependence between variables can be captured at the data level (Bracken et al., 2018).

120 There are two main approaches to estimate the unknown parameters of the conditional copula (Hochrainer-Stigler, 2020). The first one is called inference functions for margins (IFM). In this approach, the marginal distribution parameters are estimated in the first step and the copula parameters in the second step. One major disadvantage of this approach is the loss of estimation efficiency, as in the first step, the dependence between the marginal distributions is not considered. The second approach (hereafter referred to as pseudo-observations fitting) estimates the copula parameters without assuming specific

125 parametric distribution functions of the marginals, and pseudo-observations are used instead. The framework proposed here considers pseudo-observations fitting to estimate the copula dependence parameters.

2.4 Estimation strategy

Inference of the model parameters is done in a Bayesian framework, which can account for parameter uncertainties. The posterior distributions of the model parameters, $\boldsymbol{\theta} = [\boldsymbol{\mu}, \log \boldsymbol{\sigma}, \boldsymbol{\xi}]$ and $\boldsymbol{\Sigma}$, given the data (3-day spring maximum (May-June)

130 streamflow at each gauge and covariates) and considering a record length of k days by Bayes' rule, are

$$p\left(\boldsymbol{\theta}, \boldsymbol{\Sigma} \middle| \boldsymbol{q}, \boldsymbol{x}, \boldsymbol{u}\right) \propto \left[\prod_{t=1}^{k}\left(\prod_{i=1}^{m} p_q\left(q_i(t) \middle| \theta_i, \boldsymbol{x}(t)\right)\right) p_u\left(\boldsymbol{u}(t) \middle| \boldsymbol{\Sigma}\right)\right] p_\theta\left(\boldsymbol{\theta}\right) p_\Sigma\left(\boldsymbol{\Sigma}\right) \tag{8}$$

where $p_q\left(q_i(t) \middle| \theta_i, \boldsymbol{x}(t)\right)$ represents the PDF of the GEV for location i and time t, $p_u\left(\boldsymbol{u}(t) \middle| \boldsymbol{\Sigma}\right) = MVN\left(\boldsymbol{u}(t) \middle| \mathbf{0}, \boldsymbol{\Sigma}\right)$ is the Gaussian copula PDF for time t, $u(t) = [u_i(t)]_{i=1}^{m}$, $u_i(t) = \Phi^{-1}\left(F_{it}\left[q_i(t)\right]\right)$, Φ is the CDF of the standard normal distribution, $F_{it}(\cdot)$ is the empirical CDF (pseudo-observations) for location i at time t, and $p_\Sigma\left(\boldsymbol{\Sigma}\right)$ and $p_\theta\left(\boldsymbol{\theta}\right)$ represent the priors of the

135 GEV regression coefficients and Gaussian copula dependence matrix, respectively. $p_\theta\left(\boldsymbol{\theta}\right)$ is defined as

$$p_\theta\left(\boldsymbol{\theta}\right) = p_\mu\left(\boldsymbol{\mu}\right) p_\sigma\left(\log \boldsymbol{\sigma}\right) p_\xi\left(\boldsymbol{\xi}\right) \tag{9}$$

$$p_\mu\left(\boldsymbol{\mu}\right) = \prod_{j=0}^{n} MVN\left(\boldsymbol{\alpha}_{\mu_j} \middle| \mathbf{0}, \boldsymbol{\Sigma}_{\alpha_{\mu_j}}\right) p_{\Sigma_{\alpha_{\mu_j}}}\left(\boldsymbol{\Sigma}_{\alpha_{\mu_j}}\right) \tag{10}$$

$$p_\sigma\left(\log \boldsymbol{\sigma}\right) = \prod_{j=0}^{n} MVN\left(\boldsymbol{\alpha}_{\sigma_j} \middle| \mathbf{0}, \boldsymbol{\Sigma}_{\alpha_{\sigma_j}}\right) p_{\Sigma_{\alpha_{\sigma_j}}}\left(\boldsymbol{\Sigma}_{\alpha_{\sigma_j}}\right) \tag{11}$$

$$p_\xi\left(\boldsymbol{\xi}\right) = MVN\left(\boldsymbol{\alpha}_{\xi_0} \middle| \mathbf{0}, \boldsymbol{\Sigma}_{\alpha_{\xi_0}}\right) p_{\Sigma_{\alpha_{\xi_0}}}\left(\boldsymbol{\Sigma}_{\alpha_{\xi_0}}\right), \tag{12}$$

140 where $MVN\left(\boldsymbol{\alpha}_{\mu_j} \middle| \mathbf{0}, \boldsymbol{\Sigma}_{\alpha_{\mu_j}}\right)$, $MVN\left(\boldsymbol{\alpha}_{\sigma_j} \middle| \mathbf{0}, \boldsymbol{\Sigma}_{\alpha_{\sigma_j}}\right)$, and $MVN\left(\boldsymbol{\alpha}_{\xi_0} \middle| \mathbf{0}, \boldsymbol{\Sigma}_{\alpha_{\xi_0}}\right)$ represent probability densities of multivariate normal distributions with mean $\mathbf{0}$ and covariance matrices $\boldsymbol{\Sigma}_{\alpha_{\mu_j}}$, $\boldsymbol{\Sigma}_{\alpha_{\sigma_j}}$, and $\boldsymbol{\Sigma}_{\alpha_{\xi_0}}$ correspond to the priors of the GEV regression coefficients $\boldsymbol{\alpha}_{\mu_j}$, $\boldsymbol{\alpha}_{\sigma_j}$, and $\boldsymbol{\alpha}_{\xi_0}$ respectively; and $p_{\Sigma_{\alpha_{\mu_j}}}\left(\boldsymbol{\Sigma}_{\alpha_{\mu_j}}\right)$, $p_{\Sigma_{\alpha_{\sigma_j}}}\left(\boldsymbol{\Sigma}_{\alpha_{\sigma_j}}\right)$, and $p_{\Sigma_{\alpha_{\xi_0}}}\left(\boldsymbol{\Sigma}_{\alpha_{\xi_0}}\right)$ are the priors of $\boldsymbol{\Sigma}_{\alpha_{\mu_j}}$, $\boldsymbol{\Sigma}_{\alpha_{\sigma_j}}$, and $\boldsymbol{\Sigma}_{\alpha_{\xi_0}}$, which based on Gelman and Hill (2006) are assumed to follow an inverse-Wishart distribution to ensure a positive definite covariance matrix

$$\mathbf{\Sigma}_{\alpha_{\mu_j}} \sim Inv\ wishart\left(\nu, A_j\boldsymbol{I}\right) \tag{13}$$

$$\mathbf{\Sigma}_{\alpha_{\sigma_j}} \sim Inv\ wishart\left(\nu, B_j\boldsymbol{I}\right) \tag{14}$$

$$\mathbf{\Sigma}_{\alpha_{\xi_0}} \sim Inv\ wishart\left(\nu, C_0\boldsymbol{I}\right). \tag{15}$$

ν corresponds to the degrees of freedom $(m+1)$, $\boldsymbol{I}$ is an $(m+2)\times(m+2)$ identity matrix, and A_j, B_J, and C_0 are scalars properly set for $\mathbf{\Sigma}_{\alpha_{\mu_j}}$, $\mathbf{\Sigma}_{\alpha_{\sigma_j}}$, and $\mathbf{\Sigma}_{\alpha_{\xi_0}}$, respectively. The regression coefficients are modeled jointly to capture their spatial correlations. Finally, $p_{\Sigma}\left(\mathbf{\Sigma}\right)$ represents the prior of the Gaussian copula dependence matrix and is also assumed to follow an inverse-Wishart distribution to ensure a positive definite covariance matrix

$$\mathbf{\Sigma} \sim Inv\ wishart\left(\nu, \boldsymbol{C_u}\right) \tag{16}$$

where $\boldsymbol{C_u}$ corresponds to the covariance matrix of the uniform quantiles obtained from the pseudo-observations.

2.5 Estimation of ensembles of seasonal streamflow projections

The predictive posterior distribution of spring maximum streamflow (ensembles) for the m streamflow gauges can be estimated using the posterior distributions (M samples) of GEV regression coefficients, $\boldsymbol{\alpha}_{\mu_j}$, $\boldsymbol{\alpha}_{\sigma_j}$, and $\boldsymbol{\alpha}_{\xi_0}$, and the Gaussian copula dependence matrix, $\mathbf{\Sigma}$, which have been estimated using the estimation strategies presented in the previous section. To estimate spring maximum streamflow ensemble members, for each posterior sample of all model parameters ($\boldsymbol{\alpha}_{\mu_j}$, $\boldsymbol{\alpha}_{\sigma_j}$, $\boldsymbol{\alpha}_{\xi_0}$, and $\mathbf{\Sigma}$) the procedure is as follows:

1. If the posterior PDFs of the slope coefficients of the GEV parameters were found to be significant, compute the GEV parameters ($\mu_i(t)$, $\log\left(\sigma_i(t)\right)$) for each year and gauge using $\boldsymbol{\alpha}_{\mu_i}$, $\boldsymbol{\alpha}_{\sigma_i}$, and covariates, $\boldsymbol{x}(t)$, using Eq. (3)-(4).

2. Simulate marginal cumulative distributions, F_{it}, for the m streamflow gauges from a Gaussian copula with a dependence matrix, $\mathbf{\Sigma}$.

3. Compute spring maximum streamflow for each streamflow gauge i at time t using the following expression

$$q_i(t) = \mu_i(t) + \frac{\sigma_i(t)}{\xi_i}\left[\left(-\log\left(F_{it}\right)\right)^{-\xi_i} - 1\right], \quad i = 1,\ldots,m \tag{17}$$

where $\sigma_i(t) = \exp\left(\log(\sigma_i(t)\right)$

4. Repeat steps 2-4 for each gauge and year of the record.

This procedure has to be repeated M times.

3 Application of framework to the Upper Colorado River basin

We demonstrate the utility of the framework proposed in the previous section by applying it to project 3-day spring maximum (May-June) streamflow at seven gauges in the Upper Colorado River basin (UCRB) with 0 to 2 months lead time (Fig. 2). The UCRB is located in west-central Colorado, US, and has an area of approximately 25,700 km^2. Its headwaters originate at the Continental Divide in Rocky Mountain National Park. Further downstream, UCRB flows in a westerly direction through forested mountains and irrigated valleys before it leaves Colorado in Mesa County downstream of the City of Grand Junction (Colorado's Decision Support Systems, 2007). The basin has a snowmelt-dominated flow regime, i.e., most of the precipitation is accumulated during winter in the form of snow. Over 85% of the basin's streamflow and flood peaks occur in spring due to snowmelt. Therefore, using snow information of the basin might provide skillful projections of spring maximum streamflow several months in advance.

3.1 Streamflow data

Daily spring, May through June, streamflow data were obtained from the US Geological Survey (USGS) using the R package dataRetrieval (De Cicco et al., 2018). We selected streamflow gauges located inside the UCRB with no more than 10% or three consecutive years of missing data from 1965 to 2018. This procedure resulted in the selection of seven streamflow gauges (Fig. 2 and Table 1). The seven gauges have drainage areas between 14.5 and 432.5 km^2, elevations between 2105 and 3179 m.a.s.l., and mean streamflow and mean seasonal (May-June) streamflow range from 1 to 28.3 m^3 s^{-1} and from 0.3 to 8.3 m^3 s^{-1}, respectively. The seven catchments are not nested, instead they are individual sub-catchments of the larger UCRB. We computed 3-day spring maximum streamflow for each year at each streamflow gauge. For a gauge with missing annual values, these values were substituted with the gauge's median value.

Figure 3 shows the spatial dependence of 3-day spring maximum streamflow for the seven gauges, which was assessed using Kendall's rank correlation for each pair of stations. The dependence of 3-day spring maximum streamflows between gauges is generally positive as indicated by Kendall's rank correlation values higher than 0.4 (significant at 95% confidence level) for all station pairs. These significant spatial correlations require the inclusion of a copula in the BHM to capture the spatial dependence of the data.

3.2 Covariates

It has been shown in previous studies that snow water equivalent (SWE) accumulated until the beginning of spring is the most skillful predictor of spring-summer seasonal streamflow across mountainous regions, such as the western US (Koster et al., 2010; Pagano, 2010; Wood et al., 2016; Livneh and Badger, 2020). Other potentially useful predictors might include sea surface temperature anomalies or atmospheric teleconnection patterns. For the Colorado River, strong links between annual flow and large scale climate drivers have been documented – e.g., with Atlantic Multidecadal Oscillation (AMO, McCabe and Dettinger, 1999; Enfield et al., 2001; Hidalgo, 2004; Tootle et al., 2005; McCabe et al., 2007; Timilsena et al., 2009; Nowak et al., 2012), Pacific Decadal Oscillation (PDO, Hidalgo, 2004; Tootle et al., 2005; Timilsena et al., 2009), and El Nino Southern Oscillation
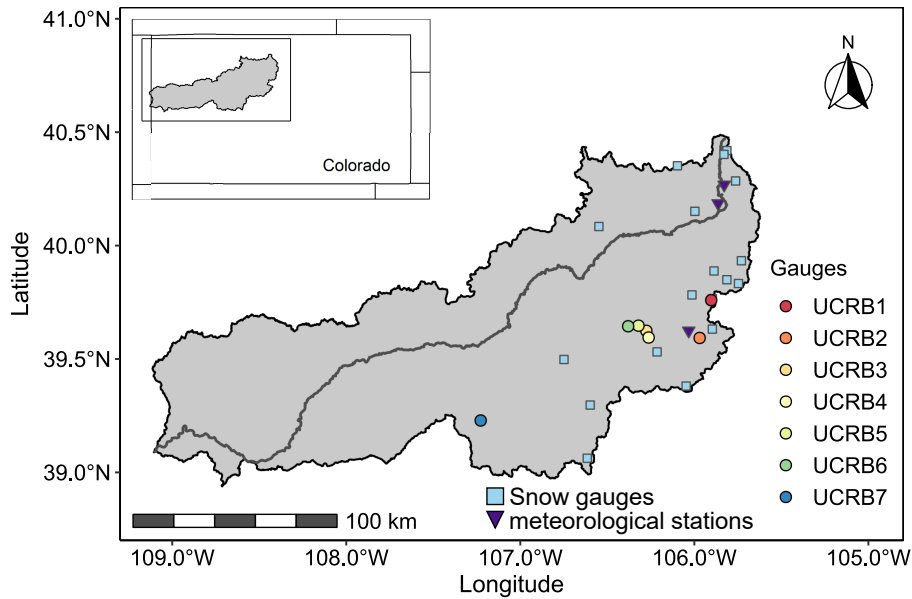
Figure 2. Streamflow gauges in the Upper Colorado River basin (UCRB) considered in this study. Light blue squares correspond to the snow gauges (18) and purple triangles to the meteorological stations (3) considered in this study.

Table 1. Basic data corresponding to the streamflow gauges in the Upper Colorado River basin (UCRB) considered in this study.

Code	USGS gauge number	River	Drainage area (km^2)	Elevation (m.a.s.l.)	Mean streamflow (m^3 s^{-1})	Mean seasonal streamflow (m^3 s^{-1})
UCRB1	9034900	Bobtail creek	14.5	3179	1.0	0.3
UCRB2	9047700	Keystone gulch	23.7	2850	0.5	0.2
UCRB3	9065500	Gore creek	37.6	2621	3.1	0.8
UCRB4	9066000	Black gore creek	32.4	2789	2.0	0.5
UCRB5	9066200	Booth creek	16.0	2537	1.3	0.3
UCRB6	9066300	Middle creek	15.4	2499	0.7	0.2
UCRB7	9081600	Crystal river	432.5	2105	28.3	8.3

(ENSO, Redmond and Koch, 1991; Kahya and Dracup, 1994; Rajagopalan et al., 2000; Thomson et al., 2003; Timilsena et al., 2009). However, the relationship of these indices with annual or seasonal extremes has not been explored in-depth and earlier studies shown modest relationships – e.g. between Southwest US seasonal or annual maximum streamflow and ENSO and PDO (Sankarasubramanian and Lall, 2003; Werner et al., 2004).

205   We test the usefulness of both snow-related and climatic drivers within the BHM framework by using SWE and different climatic indices as potential covariates of the marginal GEV distributions. Specifically, we tested the following covariates for
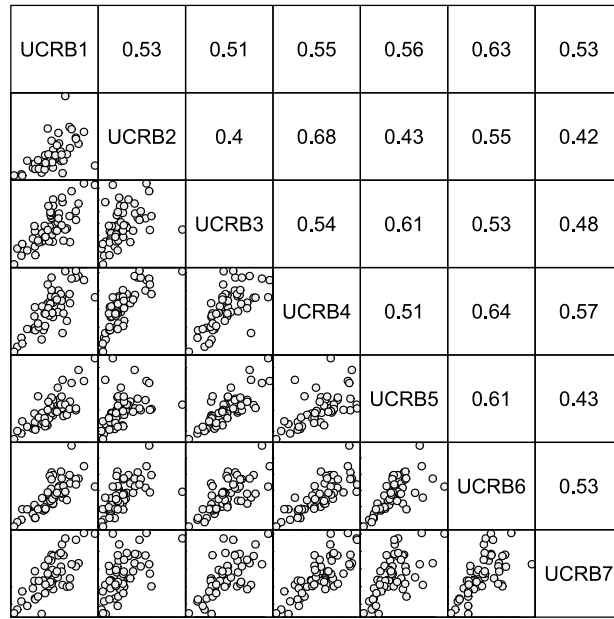
Figure 3. Pairs plot (lower triangular matrix) and Kendall's rank correlation coefficients (upper triangular matrix) of spring 3-day maximum streamflow between the 7 stations in the UCRB. Kendall's rank correlation is significant (p-values < 0.1), and positive association patterns are visible for all pairs.

modeling the temporal nonstationarity of the GEV parameters (see Eq. (3)-(4)) for the period 1965-2018: average ENSO, PDO, and AMO climate indices, spatial average of accumulated snow water equivalent (SASWE) from November to February, March, or April depending on the lead time (0, 1 or 2 months lead time), and spatial average April mean temperature (SAAMT). As indicated earlier, we focus on projecting 3-day extreme spring streamflow at lead times of 0-, 1- and 2- months lead time corresponding to forecast issuance on May 1st, April 1st and March 1st, respectively Fig. 4. The covariates use all information prior to forecast issuance. We did not consider spatial average precipitation as covariate since it can not be well predicted ahead of more than two weeks (Werner and Yeager, 2013).

The potential covariates – monthly ENSO, PDO, and AMO climate indices, monthly accumulated SWE from November to April, and daily mean temperature for April – were computed using the following data sources:

1. ENSO, PDO, and AMO climate indices: National Oceanic and Atmospheric Administration (NOAA; https://psl.noaa.gov/data/climateindices/list/);

2. SWE: Natural Resources Conservation Service (NRCS) Snow Course (https://wcc.sc.egov.usda.gov/reportGenerator/);

3. April's daily mean temperature: Global Historical Climatology Network (GHCN; Menne et al., 2012).

For SWE and daily mean temperature, we only considered snow gauges (18) and meteorological stations (3) located inside the UCRB and full record for the period of interest (1965-2018; see Fig. 2). We then computed the SASWE and SAAMT
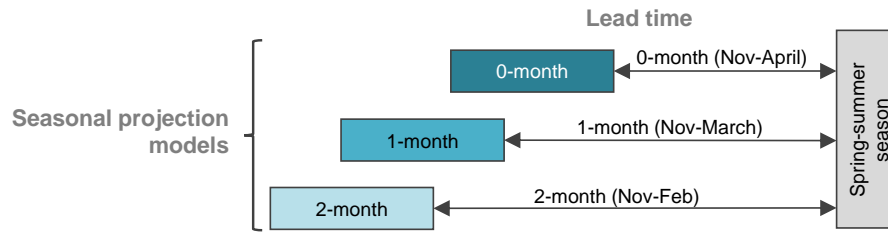
Figure 4. Schemes of nonstationary models considered for three different lead times. The dark turquoise box denotes the model for a 0-month lead time (projections are released on May 1st), the turquoise box the model for a 1-month lead time (projections are released on April 1st), and the light turquoise box the model for a 2-month lead time (projections are released on March 1st). The same color scheme will be considered for the results section.

covariates as the mean across all snow gauges and meteorological stations for each year, respectively. We considered the same SWE (SASWE) and April mean temperature (SAMAT) covariates for all the gauges because these regional variables do not rely on one single station, which may not necessarily stay in operation, and they can capture the spring maximum streamflow signal for all the station gauges. For example, suppose in the future, a particular snow gauge is out of operation. In that case, one can keep using the average of the operative snow gauges and still derive the covariate. Figure 5 displays the time series of normalized spring maximum streamflow with the SASWE (SAMAT) covariate and the best local SWE (MAT) covariate, respectively, for the station UCRB1. The two regional covariates can capture the inter-annual variability of the spring maximum streamflow without an important reduction of the correlation compared to local covariates. The suitability of the regional covariates is also verified for the other catchments and lead times.

We assessed the strength of the relationship between the covariates and spring maximum streamflow by computing the Spearman's rank correlation coefficient, which is shown in Fig. 6 for a 0-month lead time (covariates were calculated from November to April). SASWE (Fig. 6a) exhibits a significant and strong positive correlation with spring maximum streamflow at all the gauges, which was expected and also supports the choice of SASWE as a covariate for all the station gauges. At the same time, SAAMT (Fig. 6b) shows a significant negative correlation with spring maximum streamflow. This finding was also expected since a higher mean April temperature would lead to early melt and therefore less snow availability for melt later in spring. The ENSO, PDO, and AMO climate indices (Fig. 6c-e) show a weaker correlation with spring maximum streamflow than SASWE and SAAMT at almost all the gauges. Similar correlations were found for other lead times (Figs. A1 and A2). For each lead time, we obtained the best nonstationary GEV model as the combination of predictors that resulted in a minimum deviance information criterion (DIC; Spiegelhalter et al., 2002). The DIC corresponds to a hierarchical modeling generalization of the Akaike information criterion (AIC; Akaike, 2011) and facilitates Bayesian model selection. The DIC is computed for a suite of candidate models with various combinations of covariates and the model with the minimum DIC is selected for predicting spring maximum streamflow in the UCRB.
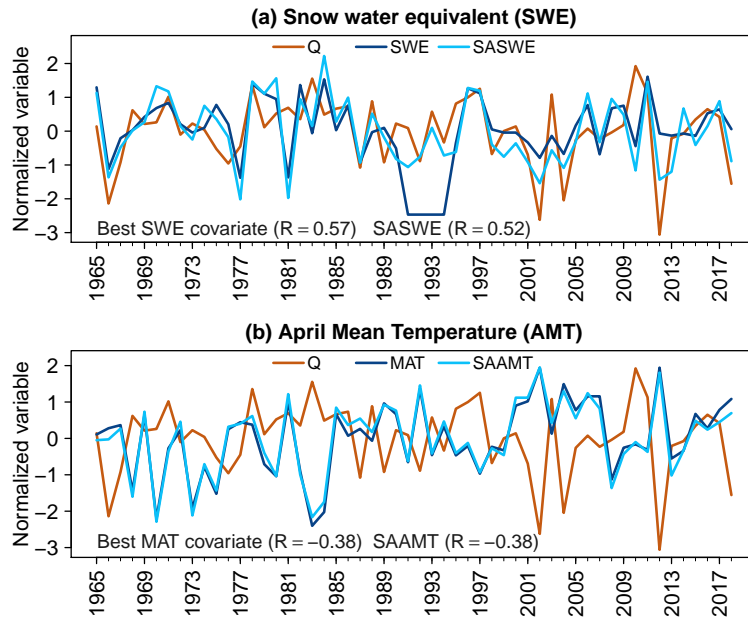
Figure 5. Times series of normalized 3-day spring maximum streamflow, best covariate, and the spatial average covariate of (a) accumulated snow water equivalent until April 30 (SWE) and (a) mean April temperature (AMT) for UCRB1. At the bottom of each panel, the correlation of 3-day maximum streamflow with the regional and the best local (i.e. highest correlation) covariate are displayed.

3.3 Suitability of the GEV distribution and Gaussian copula

245 We checked the suitability of the GEV distribution as a marginal and of the Gaussian copula as a spatial dependence model using their maximum likelihood estimates for 3-day spring maximum streamflow.

To check the validity of the GEV distribution as a marginal distribution, we fitted a stationary GEV distribution at each gauge using maximum likelihood. Then, we ran two goodness-of-fit tests, the Cramer-von Mises and Anderson-Darling tests (D'Agostino and Stephens, 1986). The p-values for the two tests were higher than 0.3 for most of the gauges, except for UCRB1

250 (0.11), which implies that at the 95% confidence level, there is insufficient evidence to reject the null hypothesis that the data come from a GEV distribution. Q-Q plots of the stationary GEV distribution fitted to 3-day spring maximum streamflow for the seven streamflow gauges of UCRB can be found in Fig. A3.

For testing the suitability of the Gaussian copula, we ran three multivariate normality tests using marginal transformations based on pseudo-observations: Royston's (Royston, 1982), Mardia's (Mardia, 1970), and Henze-Zirkler's tests (Henze and

255 Zirkler, 1990). The p-values obtained for the three tests were 0.27, 0.45, and 0.6, respectively, which did not reject the null hypothesis that the transformed data follow a multivariate normal distribution. As an illustration of the goodness fit of the Gaussian copula, Figure 7 shows the pairwise dependence structure between gauges UCRB2 and UCRB4 for different copula families (for more details about the other types of copulas, the reader is referred to Hochrainer-Stigler (2020) or Genest and
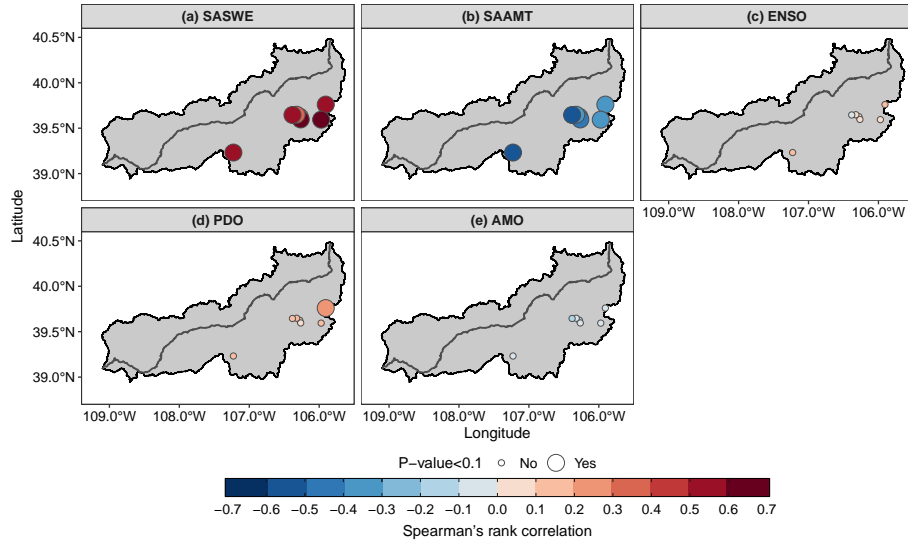
Figure 6. Spearman's rank correlation coefficient between 3-day spring maximum streamflow and potential covariates for a 0-month lead time: (a) the spatial average of Nov-April snow water equivalent (SASWE) over the UCRB; (b) the spatial average of April mean temperature (SAAMT) over the UCRB; (c) mean Nov-April ENSO; (d) mean Nov-April PDO; and (e) mean Nov-April AMO. Big circles indicate that Spearman's rank correlation is significant (p-value < 0.1).

Favre (2007)). Black points in each panel (Fig. 7b-g) correspond to the observed CDF values. The simulated contour lines
260 represent simulated contour lines for different dependence structures, including independence (no copula, Fig. 7b), Gaussian (Fig. 7c), Student-t (Fig. 7d), Joe (Fig. 7e), Gumbel (Fig. 7f), and Vine copulas (Fig. 7g). Only Gaussian, Student-t, and Vine copulas can capture the dependence structure of the data. This visual inspection confirms that the Gaussian copula is suitable to replicate the dependence structure of the observed data.

3.4 Model structure for the UCRB

265 The specific structure of the BHM for the UCRB incorporates the covariates described in section 3.2. We modeled the location parameter of the GEV at each gauge in a nonstationary way but the scale parameter of the GEV is kept stationary for all gauges. An initial run of the BHM with a nonstationary scale parameter showed that the regression coefficients ($\boldsymbol{\alpha}_{\sigma_j} = 0$ for $j > 0$ in Eq.(4)) were not significant (posterior PDFs contain zero in the 95% credible interval). The priors of the covariance matrix of $\boldsymbol{\alpha}_{\mu_j}$, $\boldsymbol{\alpha}_{\sigma_0}$, and $\boldsymbol{\alpha}_{\xi_0}$ used are:
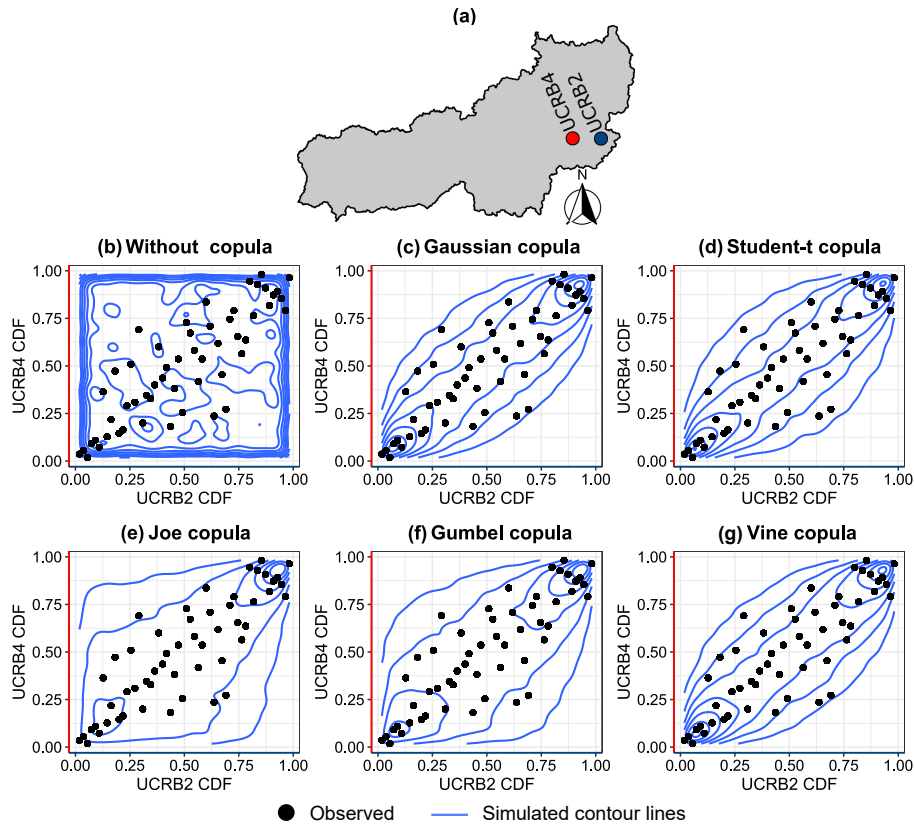
Figure 7. Pairwise dependence structure between UCRB2 and UCRB4 (a) streamflow simulated (b) without a copula and with a (c) Gaussian copula; (d) Student-t copula; (e) Joe copula; (f) Gumbel copula; and (g) Vine copula. Observations and simulated contour lines are shown as black points and blue lines, respectively.

$$\boldsymbol{\Sigma}_{\alpha_{\mu_0}} \sim Inv\ wishart\,(8, A_0 \boldsymbol{I}) \tag{18}$$

$$\boldsymbol{\Sigma}_{\alpha_{\mu_j}} \sim Inv\ wishart\,(8, A_j \boldsymbol{I}), \quad j \geq 1 \tag{19}$$

$$\boldsymbol{\Sigma}_{\alpha_{\sigma_0}} \sim Inv\ wishart\,(8, B_0 \boldsymbol{I}) \tag{20}$$

$$\boldsymbol{\Sigma}_{\alpha_{\xi_0}} \sim Inv\ wishart\,(8, C_0 \boldsymbol{I}) \tag{21}$$

We considered noninformative priors for the covariance matrix of the GEV regression coefficients by setting $A_0 = 100$, $A_j = 10$, $B_0 = 1$, and $C_0 = 1$. Since we fitted different types of BHMs, $\boldsymbol{\Sigma}_{\alpha_j}$ is only considered for nonstationary models. For the dependence matrix of the Gaussian copula, we used an informative prior

$$\boldsymbol{\Sigma} \sim Inv\ wishart\,(8, \boldsymbol{C_u}) \tag{22}$$

where $\boldsymbol{C_u}$ corresponds to the covariance matrix of the uniform quantiles obtained from the pseudo-observations of spring maximum streamflow.

3.5 Implementation and model fitting

The model was implemented in R (R Core, 2017) using the program JAGS (Just Another Gibbs Sampler; Plummer, 2003) and the R package rjags (Plummer, 2019), which provides an interface from R to the JAGS library for Bayesian data analysis. Posterior distributions of the GEV regression coefficients and Gaussian copula matrix were estimated using Gibbs sampling (Gelman and Hill, 2006; Robert and Casella, 2011) based on the priors assigned in the previous section. The predictive posterior distributions of spring maximum streamflow (ensembles) for all years were estimated according to section 2.5. We ran three parallel chains with different initial values and each simulation was performed for 2,000,000 iterations with a burn-in size value of 1,000,000 to ensure convergence. To reduce the sample dependence (autocorrelation), the thinning factor was set to 500, which yields 6000 samples (2000 samples from each chain). The scale reduction factor $\hat{R}$ (Gelman and Rubin, 1992) was used to check for model convergence, i.e., $\hat{R}$ values less than the critical value of 1.1 suggest adequate convergence of the model. In all of our runs, the $\hat{R}$ values were less than 1.1 in 6000 samples, indicating convergence. Consequently, the posterior distributions of the GEV regression coefficients, the Gaussian copula matrix, and the predictive posterior distributions of spring maximum streamflow consisted of 6000 ensembles.

3.6 Model cross-validation and verification metrics

To test the out-of-sample predictability of the model, we performed leave-one-year-out cross-validation by dropping one year from the record (1965–2018) and fitting the BHM using the remaining years, also known as the calibration years. The fitted model is applied to provide estimates for the one validation year. This cross-validation procedure was repeated 54 times.

As the goal of this study is to provide seasonal streamflow extremes projections for risk-based flood adaptation, we also implemented this leave-one-year-out cross-validation just for high-flow years in which all the station gauges exceeded their 60th percentile.

We computed the energy skill score (ESS) as our verification metric since we are interested in capturing the spatio-temporal dependence of the data. The energy score (ES) assesses probabilistic forecasts of a multivariate quantity (Gneiting and Raftery, 2007; Gneiting et al., 2008):

$$\text{ES} = \frac{1}{M} \sum_{j=1}^{M} ||\boldsymbol{q}_j - \boldsymbol{q}_o|| - \frac{1}{2M^2} \sum_{i=1}^{M} \sum_{j=1}^{M} ||\boldsymbol{q}_i - \boldsymbol{q}_j|| \tag{23}$$

where $M = 3000$ is the size of the ensemble forecast, $\boldsymbol{q}_j$ is the 7×1 vector of the jth ensemble forecast at year t, $\boldsymbol{q}_o$ is the 7×1 vector of observed streamflow at year t, and $|| \cdot ||$ denotes the Euclidean norm. This performance metric is a direct generalization of the continuous ranked probability score (CRPS; Gneiting and Raftery, 2007; Gneiting et al., 2008), to which the energy score reduces in dimension $d = 1$. Based on ES, the energy skill score (ESS) is defined as

$$\mathrm{ESS} = 1 - \frac{\overline{\mathrm{ES}}_{\mathrm{projection}}}{\overline{\mathrm{ES}}_{\mathrm{reference}}} \tag{24}$$

where $\overline{\mathrm{ES}}_{\mathrm{projection}}$ is the mean ES of the projection model analyzed and $\overline{\mathrm{ES}}_{\mathrm{reference}}$ is the mean ES of the reference projec-
tion. The ESS ranges from $-\infty$ to 1. ESS < 0 indicate that the reference projection has higher skill than the projection model,
ESS = 0 implies equal skill, and ESS > 0 means that the projection model has a higher skill, with ESS = 1 representing a
perfect score. For this study, we considered the climatology (sampling from the observations) as the reference projection and
benchmark. ESS was computed for both the calibration and validation models.

4 Results

4.1 Selection of the best model for each lead time

For each lead time, different candidate BHMs were calibrated for the period 1965–2018, and the best BHM was selected based
on the lowest DIC value. Table 2 shows DIC values for different candidate BHMs for a 0-month lead time and the best model
for the other two lead times (last two rows). In the case of a 0-month lead time, the best model corresponds to the first row of
Table 2. For a 0-month lead time, predictive skill resides in SWE and air temperature as this hydro-climatic information relates
well to the streamflow extremes in May-June (see Fig. 6). However, for longer lead times of 1 and 2-months, the large-scale
climate indices add predictive value. All the models fitted consider a Gaussian copula to model spatial dependence. Detailed
tables with different models fitted for 1-month and 2-months lead times can be found in Tables A1 and A2.

4.2 Ability of the BHM to capture spatio-temporal dependence

To assess the ability of the BHM in capturing spatio-temporal dependence through nonstationary covariates and a Gaussian
copula, we compared the best model for the 0-month lead time selected in the previous section (i.e., SASWE and SAAMT as
covariates with a Gaussian copula) against three models that do not consider a Gaussian copula: Stationary, nonstationary with
SASWE as covariate, and nonstationary with SASWE and SAAMT as covariates.

Figure 8 shows the Energy Skill Score (ESS) distribution from the calibration (1965-2018) for the four BHMs for a 0-month
lead time. Higher values of the ESS indicate better performance. The stationary model (light grey box) performs poorly in
capturing the spatio-temporal dependence compared to the benchmark (i.e., values below 0). This model also shows a lower
variability of the skill score than the other Bayesian hierarchical models, which is expected because the stationary model
produces the same projection for each year. When a nonstationary model with SASWE as a covariate is considered (grey box),
the skill is substantially improved compared to the benchmark and the stationary model (i.e., most of the values above 0). This
improvement is consistent with Fig. 6 and previous studies stating that SWE until the beginning of the spring season is the
most skillful predictor of spring-summer seasonal streamflow in mountainous regions (Koster et al., 2010; Livneh and Badger,
2020). When SAAMT is added as a covariate (dark grey box), there is a significant improvement of ESS compared to the model

Table 2. DIC values for different candidate BHMs for a 0-month lead time and the best model for the other two lead times. For each model, the same covariates for the location parameter are considered at all gauges. Candidate BHMs are sorted from the lowest to the highest DIC value for a 0-month lead time. Scale and shape parameters are considered stationary. All candidate BHMs consider a Gaussian copula to model spatial dependence.

Lead time	Model	Covariates	DIC
0-month	Nonstationary	SASWE, SAAMT	1021.5
	Nonstationary	SASWE, AMO, SAAMT	1030.9
	Nonstationary	SASWE, ENSO, SAAMT	1032.7
	Nonstationary	SASWE, PDO, SAAMT	1032.7
	Nonstationary	SASWE	1034.5
	Nonstationary	SASWE, ENSO, AMO	1045.3
	Nonstationary	SASWE, PDO, AMO	1047.6
	Nonstationary	SASWE, ENSO, PDO	1049.7
	Nonstationary	SASWE, ENSO	1077.8
	Stationary	–	1132.8
	Nonstationary	SASWE, AMO	1151.4
	Nonstationary	SASWE, PDO	1173
1-month	Nonstationary	SASWE, PDO	1065.2
2-months	Nonstationary	SASWE, ENSO	1075.6

with only SASWE. The best model with copula (dark turquoise box) substantially increases model skill. Model skill increases were tested with a 95 % confidence interval using a nonparametric test for the median (Gibbons and Chakraborti, 1992).

To further highlight the ability of the Gaussian copula to capture spatio-temporal dependence, we computed spatial joint threshold non-exceedance probabilities for the seven stations and compared them to non-exceedance probabilities derived from three models without the copula, i.e., spatially independent models for each streamflow gauge. In Figure 9, we display the distribution of the probability that all streamflow gauges do not exceed their kth percentile for the observations and the four models shown in Fig. 8 for a 0-month lead time and the calibration period. The model with nonstationary covariates and a Gaussian copula (dark turquoise box plots) can almost reproduce the shape of the observed distribution in terms of the inter-quartile range (boxes), which is an indication that this model can capture the spatio-temporal dependence of the data well. Figure 9 also shows that even without considering a copula, a nonstationary model with skillful covariates can partially capture the spatio-temporal dependence (see in Fig. 9 the difference of the distribution shape for the stationary and nonstationary models without copula). The ability of nonstationry model to partially capture the spatio-temporal dependence suggests that with increasing skill of the covariates, the added value of the copula gets smaller. Similar performance was observed for the nonstationary model with SASWE as a covariate plus a Gaussian copula and for a nonstationary model with a less skillful covariate (ENSO) plus a Gaussian copula (not shown here).
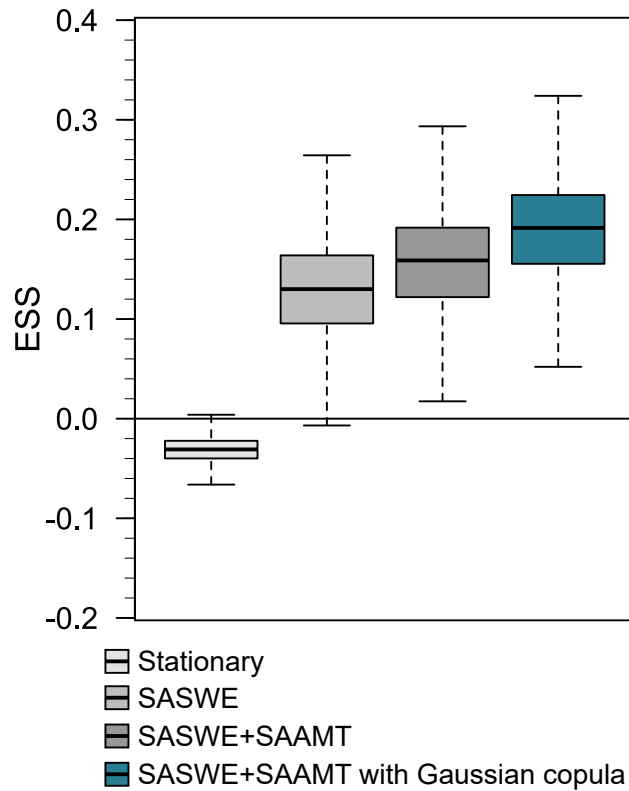
Figure 8. Energy Skill Score (ESS) distribution for four different BHM versions for a 0-month lead time for the calibration period (1965–2018). Higher values of the ESS indicate better model performance. The whiskers show the 95% credible intervals, boxes the inter-quartile range, and horizontal lines inside the boxes, the median. Outliers are not displayed. The light grey box denotes a stationary model, the grey box a nonstationary model with SASWE as a covariate, the dark grey box a nonstationary model with SASWE and SAAMT as covariates, and the dark turquoise model adds a Gaussian copula to model spatial dependence.

In order to assess the spatial performance of the BHM, Figure 10 shows the time series of the spatial average projection of maximum specific streamflow in spring over all seven gauges of the UCRB from the calibration (1965–2018) for the best model for a 0-month lead time without a Gaussian copula and with a Gaussian copula, respectively. Our results show that 355 by adding a Gaussian copula to the BHM (Fig. 10b), observations can be better captured by the ensembles' median; and the ensembles represent a higher variability, which allows for capturing some observations that are not captured without the copula (Fig. 10a). For the remainder of this paper, we use the term "average projection of spring maximum specific streamflow" to refer to spatial average projection of spring maximum specific streamflow over all seven gauges of the UCRB.
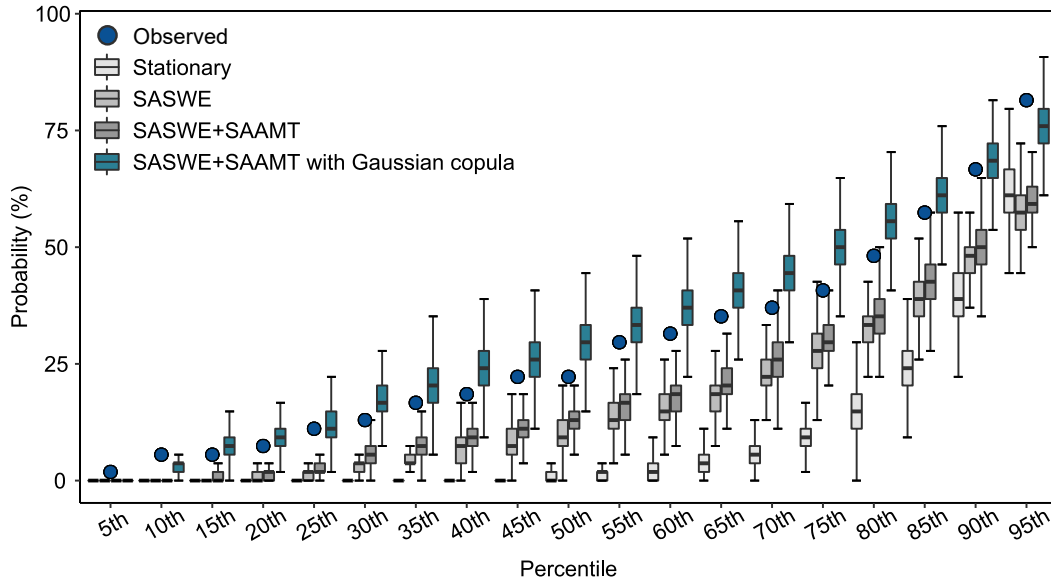
Figure 9. Distribution of the probability that all gauges do not exceed their kth percentile for four different versions of the BHM for a 0-month lead time for the calibration period (1965–2018). The whiskers show the 95% credible intervals, boxes the inter-quartile range, and horizontal lines inside the boxes, the median. Outliers are not displayed. The observations are shown as blue circles and the same color scheme as in Fig. 8 is considered for the four versions of the BHM.

4.3 Model performance at different lead times

360 To define the extent to which seasonal streamflow extremes projections for longer lead times can be skillful, we assess the performance of the BHM at different lead times for the calibration and leave-1-year-out cross-validation, including cross-validation focusing on extremes (60th percentile). Covariates considered for each lead time were presented in section 4.1.

Figure 11 displays the Energy Skill Score (ESS) distribution for different lead times from calibration, leave-1-year-out cross-validation, and leave-1-year-out cross-validation on extremes. EES decreases as the lead time increases indicating a decrease

365 of model skill with increasing lead time (Fig. 11a). However, the three lead times capture the multivariate dependence better than the calibration benchmark (ESS values above 0). For the leave-1-year-out cross-validation (Fig. 11b), there is a substantial decrease in performance compared to the calibration, except for the 0-month lead time (dark turquoise boxplot). However, model performance for the 1-month lead time is better than the benchmark (ESS quartiles above 0), and the model for a 2-months lead time shows lower performance than the benchmark only for the third quartile (above 0). Finally, for the leave-

370 1-year-out validation for extremes (Fig. 11c), all lead times show higher skill than the benchmark (ESS quartiles above 0), highlighting the potential usefulness of the model for flood risk assessments.

To assess at site performance, we computed the continuous rank probability skill score (CRPS; Hersbach, 2000; Gneiting and Raftery, 2007) at each gauge (see Fig. A4). As for the ESS, the CRPSS ranges from $-\infty$ to 1, and its values have the same
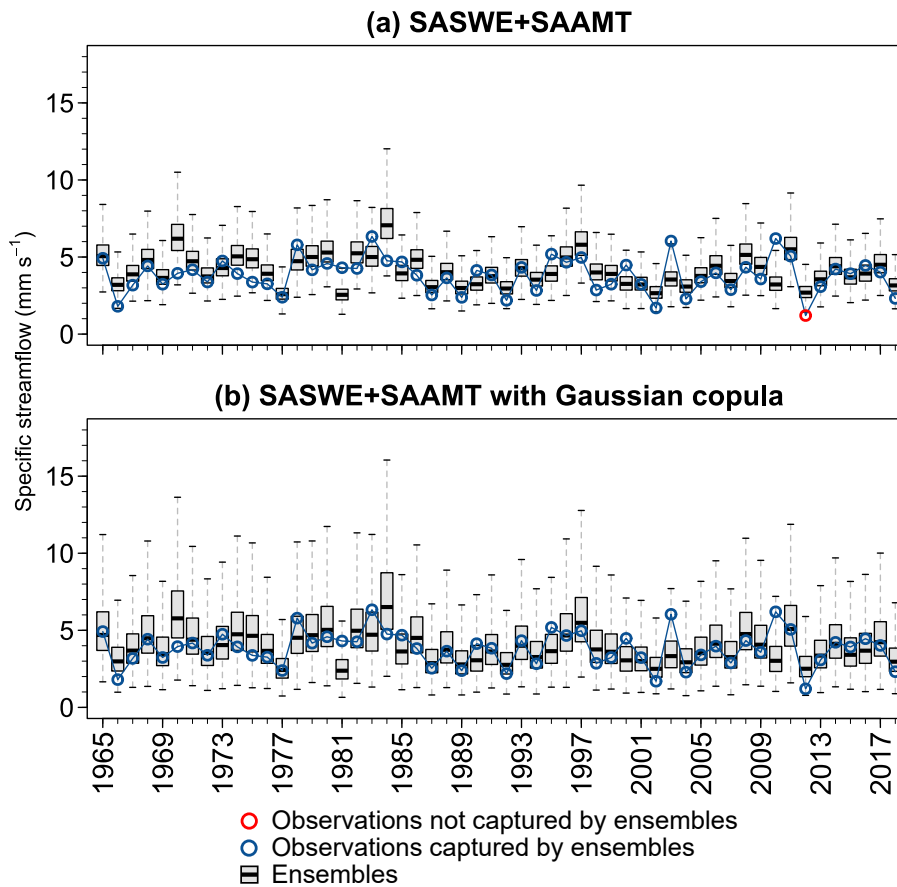
Figure 10. Time series of average projected spring maximum specific streamflow over all seven gauges of the UCRB $(\mathrm{mm\,d^{-1}})$ from the calibration (1965–2018) for the best model for a 0-month lead time (a) without a Gaussian copula and (b) with a Gaussian copula. Blue and red points indicate observations captured or not by the ensemble's variability, respectively. Whiskers indicate the 95% credible intervals, boxes the inter-quartile range, and horizontal lines inside the boxes, the median. Outliers are not displayed. Ensemble refers to the set of projections produced for each year.

meaning (see section 3.6). We obtained similar results to ESS (Fig. 11) with the exception of a few gauges for leave-1-year-out cross-validation and leave-1-year-out cross-validation for extremes where the performance was poorer than the benchmark for the cross-validation.

Figure 12 shows the time series of average projected spring maximum specific streamflow ensembles and the distributions of the Pearson correlation coefficient from the leave-1-year-out cross-validation for the three lead times and the benchmark. Simulations relying on models with a copula show a similar variability and can capture observed values inside of their ensembles' variability for all three lead times (Fig. 12a-b). The benchmark (Fig. 12d) cannot capture the observations since it converges to a stationary model, i.e., it gives the same projection for all years. There is a slight performance reduction for models with 1- and 2-months lead times compared to the 0-month lead time (Fig. 12e). The medians of the Pearson correlation
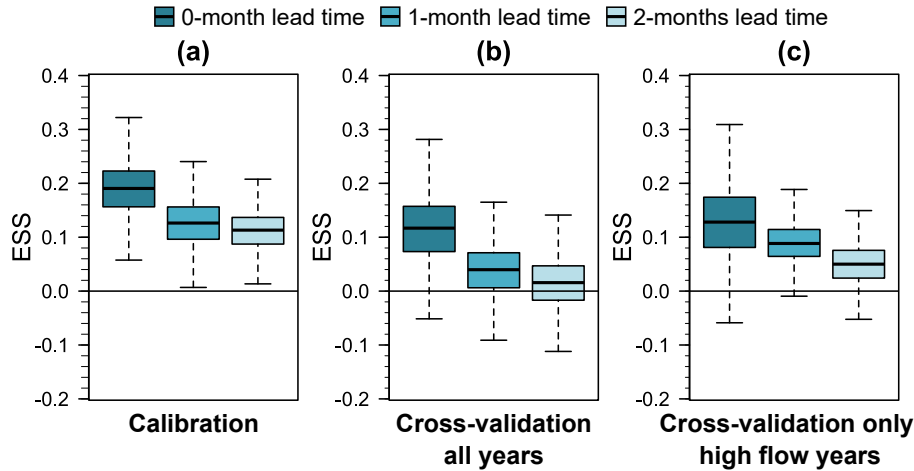
Figure 11. Energy Skill Score (ESS) distribution for different lead times from (a) calibration; (b) leave-1-year-out cross-validation; and (c) leave-1-year-out cross-validation for extremes (60th percentile). Dark turquoise boxplots denote a 0-month lead time, turquoise boxplots a 1-month lead time, and light turquoise boxplots a 2-months lead time. Higher values of the ESS indicate better model performance. Whiskers indicate the 95% credible intervals, boxes the inter-quartile range, and the horizontal lines inside the boxes, the median. Outliers are not displayed. All the models consider a Gaussian copula.

coefficient for the three lead times vary between 0.37 and 0.5 while the median for the benchmark is close to -1. In addition, model performance for the calibration (see Fig. A5) is similar to the one of the cross-validation. This result indicates only small performance reductions for projections and implies that the framework proposed could be useful for the early implementation of flood risk adaptation strategies each year.

5 Discussion

Compared to operational forecast models that consider short lead times and seasonal streamflow forecast models that are useful for reservoir operation with a focus on water availability during the dry season, the proposed BHM proposed here has the following benefits:

- It allows for considering potential climate change effects by modeling the margins in a nonstationary setting using suitable covariates.

- It allows for capturing spatio-temporal dependence by including a Gaussian copula. Consequently, the spatial BHM captures observations that are not captured by the average projection of spring maximum specific streamflow of a BHM without a copula.

- It provides average projections of spring maximum specific streamflow up to 2-months in advance by relying on the predictive skill of snow accumulated during the winter season.
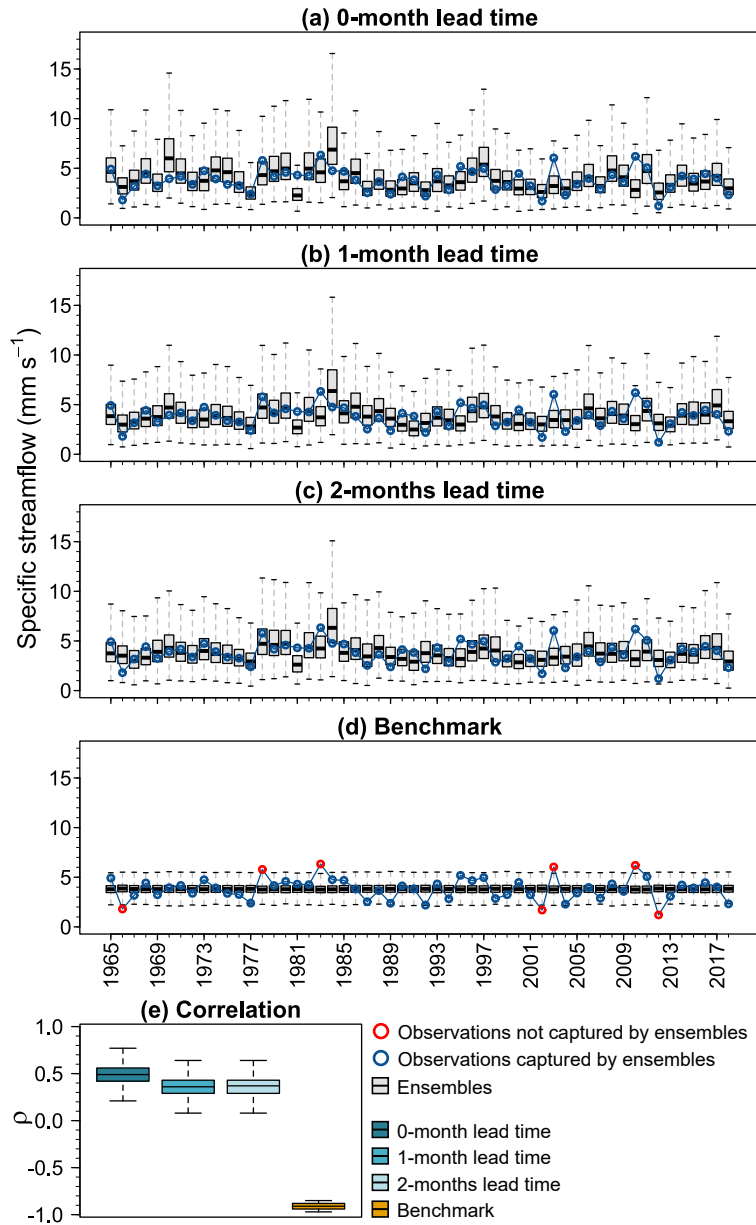
Figure 12. Time series of average projected spring maximum specific streamflow, $(mm\,d^{-1})$, from the leave-1-year-out cross-validation for a (a) 0-month lead time; (b) 1-month lead time; (c) 2-months lead time; (d) benchmark; and (e) distributions of the Pearson correlation coefficient between observed and ensembles of average projection spring maximum specific streamflow over all seven gauges for the different models. Blue and red points in panels (a) – (d) indicate when observations are captured or not by the ensembles' variability, respectively. Whiskers show the 95% credible intervals, boxes the inter-quartile range, and horizontal lines inside the boxes, the median. Outliers are not displayed. All lead time models consider a Gaussian copula.

A question coming to mind is: how can the proposed modeling framework be used to deliver interpretable seasonal average projections? It might be difficult for decision-makers to make decisions based on average spring maximum specific streamflow over all seven gauges of the UCRB (see Fig. 12). To overcome this difficulty, we propose to provide interpretable average projections of spring maximum specific streamflow by providing the first three quartiles of the ensembles along with some past streamflow values as a reference. Providing reference values can help to make decisions about risk adaptation up to two months in advance. Reference values can be, e.g., the observed median specific streamflow for an average year without flood occurrence; the maximum observed specific streamflow on the record; or the lowest observed specific streamflow (threshold) that can cause flood occurrence. To find the threshold flow that can cause flood occurrence, we computed the ratio between average maximum and average spring mean specific streamflow over all seven gauges of the UCRB. Then, we picked the average spring maximum specific streamflow value of the year with the highest ratio value, which corresponds to the threshold streamflow. The reason for this is that when the basin is drier (high ratio between peak runoff and total seasonal runoff), even if the peak streamflow is not so high, a flood can occur. Based on the lowest observed specific streamflow (threshold, q_{thresh}) that can trigger flood occurrence we define a potential flooding alarm system. This system defines different flooding alarm levels by comparing the threshold against the first three quartiles (exceedance probability, q_{25th}, q_{50th}, and q_{75th}) of average projections of spring maximum specific streamflow for the year analyzed. This potential flooding alarm system is shown in Fig. 13a. Thus, for each lead time, the flooding alarm is activated with a low risk of flooding if $q_{25th} > q_{thresh}$; moderate risk of flooding if $q_{50th} > q_{thresh}$; or high risk of flooding if $q_{25th} > q_{thresh}$. In all other cases, the alarm is not activated.

To illustrate this system, Figure 13b-c shows examples of when the potential flooding alarm is successfully activated or not activated. Figure 13b presents the average projections of spring maximum specific streamflow of the UCRB for 2011 at three lead times (0-2 months), which were obtained from the leave-1-year-out cross-validation, along with the three reference values mentioned above and the observed value for 2011. It can be seen that based on the average projections, The flooding alarm is activated with a low risk of flooding by March 1st (2-months lead time), moderate risk of flooding by April 1st (1-month lead time), and high risk of flooding by May 1st (0-month lead time). Thus, the flooding alarm is successfully activated before spring since the observed value for 2011 exceeded the threshold streamflow, and actually, flood impacts were documented in 2011 (Werner and Yeager, 2013). In addition, Figure 13c shows the average projection of spring maximum specific streamflow of the UCRB for 2018 when the flooding alarm is successfully not activated because the three quartiles for each lead time and the observed streamflow for 2018 are below the threshold streamflow.

The nonstationary and spatial BHM framework proposed here was applied to the UCRB using 3-day maxima. However, the framework is flexible and can be applied to other types of maxima such as 1-day maxima, be implemented in other regions, be applied to other types of extremes such as droughts, or be used under future climate conditions. In order to apply the framework in another variable or region, the choice of covariates has to be reconsidered and potentially adjusted. In the application presented here, we only modeled the location parameter as nonstationary. If the framework is applied to another basin, this modeling choice has to be reconsidered. It is advisable as a first step to do an initial run of the model for defining which parameters should be considered nonstationary. If one wishes to apply the framework to predict another type of extreme such as low-flows, one needs to reconsider distribution choice and to identify suitable covariates. In addition, the framework is not
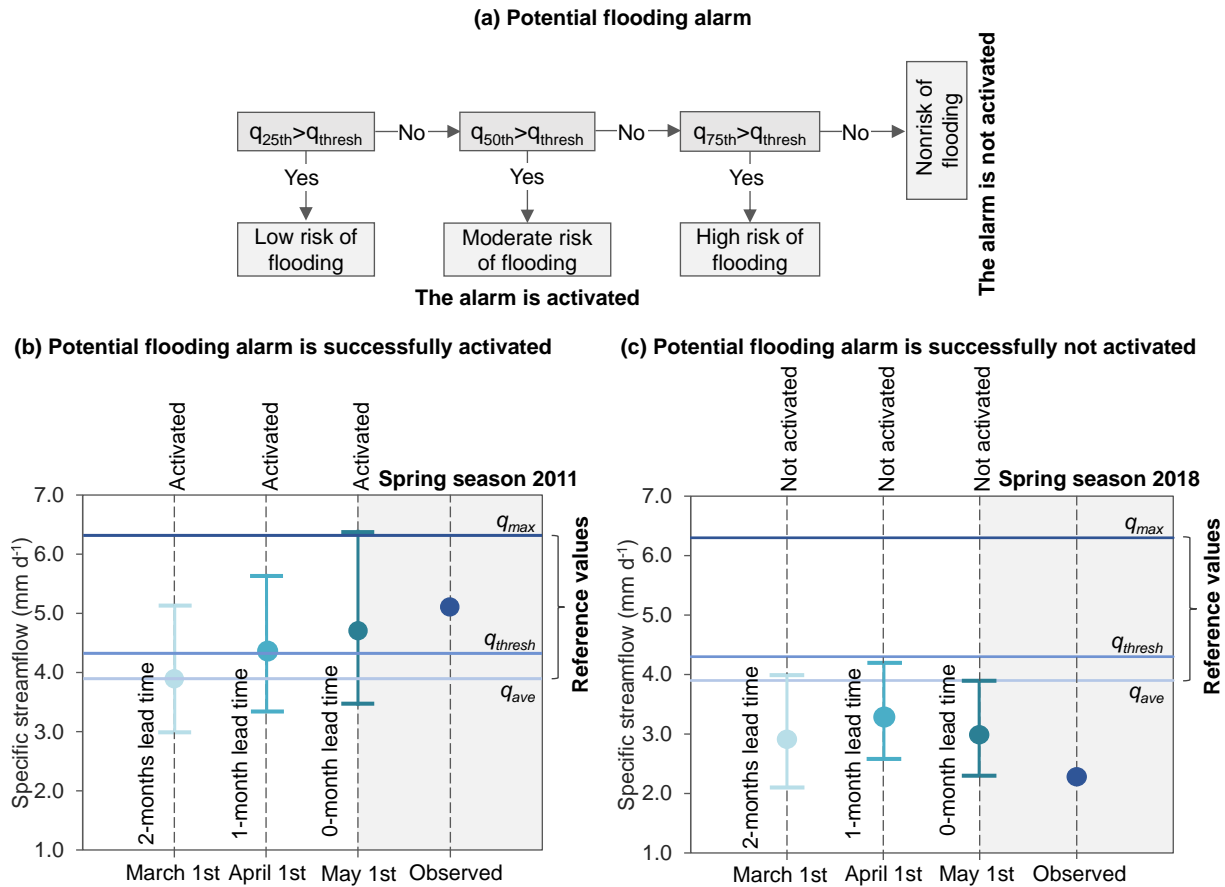
Figure 13. (a) Schematic of the potential flooding alarm system proposed. The flooding alarm is activated if $q_{25th} > q_{thresh}$ (low risk of flooding), $q_{50th} > q_{thresh}$ (moderate risk of flooding), or $q_{75th} > q_{thresh}$ (high risk of flooding). Otherwise, the alarm is not activated. (b) average projections of spring maximum specific streamflow of UCRB for 2011 when flooding is successfully activated, and (c) average projections of spring maximum specific streamflow of UCRB for 2018 when flooding is successfully not activated. average projections at a 0-, 1-, and 2-months lead times correspond to dark turquoise, turquoise, and light turquoise, respectively. The blue point corresponds to the observed specific streamflow for 2018, horizontal lines correspond to the observed highest specific streamflow (q_{max}, dark blue), observed flooding threshold specific streamflow (q_{thresh}, blue), and observed average specific streamflow (q_{ave}, light blue). For each lead time, the whiskers show the first and third quartile (q_{25th} and q_{75th}), the point, the median or second quartile (q_{50th}).

limited to projections, it can also be adapted for simulation purposes by considering real-time covariates. In addition, it can be easily adjusted such that it represents future climate conditions if future projections of the covariates are available. However, the predictive skill of the model fitted and applied to the UCRB may change under future climate conditions. The relative importance of snowmelt and precipitation in causing flood events may change in the future, with precipitation becoming relatively more important. Consequently, the model's predictive skill, which heavily relies on SWE as a covariate, might slightly decrease in future. However, in the case of headwater basins in mountain regions such as the one considered in this

study, snowmelt will remain the dominant flood generation process in the future, as shown by climate change projections in the region (Safeeq et al., 2016). Under changing conditions, one may want to reconsider covariate choice and test additional potentially skillful covariates such as specific ocean and atmosphere features that are expected to have a stronger relationship with the basin streamflow and extremes (e.g.; Grantz et al., 2005; Regonda et al., 2006; Bracken et al., 2010). Although this framework can be applied to a more extensive stream gauges network, we do not recommend that since clusters of different streamflow behavior will develop as the size of the region of interest increases. In that case, it is more efficient to fit a model for each cluster than to fit a model for the entire region, which will be more computationally expensive. Fitting a model for each cluster allows for using different covariates for each cluster, which may help to provide more skillful estimates than the non-cluster case.

6 Summary and conclusions

In this study, we presented a Bayesian Hierarchical Model (BHM) to project seasonal streamflow extremes for several catchments in a river basin for several lead times. The streamflow extremes at a number of gauges in a basin are modeled using a Gaussian elliptical copula and Generalized Extreme Value (GEV) margins with nonstationary parameters. These parameters are modeled as a linear function of suitable covariates from the previous season.

We applied this framework to project 3-day spring maximum (May-June) streamflow at seven gauges in the Upper Colorado River Basin (UCRB) network, at 0-, 1-, and 2-months lead time. As potential covariates, we used indices of large-scale climate teleconnections – ENSO, AMO, and PDO, regional mean snow water equivalent, and temperature from the preceding winter season.

From the analysis of different models for a 0-month lead time, we conclude that:

– The spatial average snow water equivalent (SASWE) accumulated during fall and spring is the most skillful predictor of spring season maximum streamflow across the UCRB.

– The increase in BHM performance is low when adding other climatic indices such as PDO.

– Including a copula in the BHM enables capturing the spatio-temporal dependence of streamflow extremes which is not fully possible with independent marginal models.

The comparative analysis for three different lead times revealed that increasing the lead time from 0 to 2 months only weakly decreases model skill. This finding implies that the framework proposed could be useful for the early implementation of flood risk adaptation and preparedness strategies. We propose an alternative to guide decision making by providing average projections of spring maximum specific streamflow as the first three quartiles of the ensembles of the average projection of spring maximum specific streamflow along with past observed specific streamflow values as reference. Such a communication strategy could help decision-makers to implement adaptation strategies that address the spatial dimension of flooding.

Data availability. The dataset used in this study, which consists of time series of potential covariates and 3-day spring maximum streamflow for the seven station gauges, can be downloaded from HydroShare https://doi.org/10.4211/hs.d8c1b413951843cf9be968e9d2a4aa79

Author contributions. The idea and setup for the paper were jointly developed by the four co-authors. The model implementation and analysis were performed by AO and discussed with the co-authors. AO wrote the first draft of the manuscript which was revised and edited by MIB, RB, and WK.

Competing interests. The authors declare that they have no conflict of interest.

Acknowledgements. This project was funded by the National Science Foundation grant 1243270. We also acknowledge the support from the Fulbright Foreign Student Program and the Comisión Nacional de Investigación Científica y Tecnológica (CONICYT) Scholarship Program/DOCTORADO BECAS CHILE/2015-56150013 for the first author. The second author was supported by the Swiss National Science Foundation via a PostDoc.Mobility grant (Number: P400P2_183844). Partial support from the Monsoon Mission Project of the Ministry of Earth Sciences, India, for first and second authors is thankfully acknowledged. The fourth author was supported by NSF DMS-1811294 and DMS-1923062.

References

Akaike, H.: Akaike's Information Criterion, p. 25, Springer Berlin Heidelberg, Berlin, Heidelberg, https://doi.org/10.1007/978-3-642-04898-2_110, 2011.

Anghileri, D., Voisin, N., Castelletti, A., Pianosi, F., Nijssen, B., and Lettenmaier, D. P.: Value of long-term streamflow forecasts to reservoir operations for water supply in snow-dominated river catchments, Water Resources Research, 52, 4209–4225, https://doi.org/10.1002/2015WR017864, 2016.

Apputhurai, P. and Stephenson, A. G.: Spatiotemporal hierarchical modelling of extreme precipitation in Western Australia using anisotropic Gaussian random fields, Environmental and Ecological Statistics, 20, 667–677, https://doi.org/10.1007/s10651-013-0240-9, 2013.

Atyeo, J. and Walshaw, D.: A region-based hierarchical model for extreme rainfall over the UK, incorporating spatial dependence and temporal trend, Environmetrics, 23, 509–521, https://doi.org/10.1002/env.2155, 2012.

Bracken, C., Rajagopalan, B., and Prairie, J.: A multisite seasonal ensemble streamflow forecasting technique, Water Resources Research, 46, https://doi.org/10.1029/2009WR007965, 2010.

Bracken, C., Rajagopalan, B., and Woodhouse, C.: A Bayesian hierarchical nonhomogeneous hidden Markov model for multisite streamflow reconstructions, Water Resources Research, 52, 7837–7850, https://doi.org/10.1002/2016WR018887, 2016.

Bracken, C., Holman, K. D., Rajagopalan, B., and Moradkhani, H.: A Bayesian Hierarchical Approach to Multivariate Nonstationary Hydrologic Frequency Analysis, Water Resources Research, 54, 243–255, https://doi.org/10.1002/2017WR020403, 2018.

Brunner, M. I., Furrer, R., and Favre, A.-C.: Modeling the spatial dependence of floods using the Fisher copula, Hydrology and Earth System Sciences, 23, 107–124, https://doi.org/10.5194/hess-23-107-2019, 2019.

Brunner, M. I., Papalexiou, S., Clark, M. P., and Gilleland, E.: How Probable Is Widespread Flooding in the United States?, Water Resources Research, 56, e2020WR028 096, https://doi.org/10.1029/2020WR028096, 2020.

Chen, L., Zhang, Y., Zhou, J., Singh, V. P., Guo, S., and Zhang, J.: Real-time error correction method combined with combination flood forecasting technique for improving the accuracy of flood forecasting, Journal of Hydrology, 521, 157–169, https://doi.org/10.1016/j.jhydrol.2014.11.053, 2015.

Clark, M. P. and Hay, L. E.: Use of medium-range numerical weather prediction model output to produce forecasts of streamflow, Journal of Hydrometeorology, 5, 15–32, https://doi.org/10.1175/1525-7541(2004)005<0015:UOMNWP>2.0.CO;2, 2004.

Coles, S.: An introduction to statistical modeling of extreme values, Springer, London, 2001.

Colorado's Decision Support Systems: Upper Colorado River Basin Information, Tech. rep., Colorado Water Conservation Board, 2007.

Cooley, D. and Sain, S. R.: Spatial hierarchical modeling of precipitation extremes from a regional climate model, Journal of Agricultural, Biological, and Environmental Statistics, 15, 381–402, https://doi.org/10.1007/s13253-010-0023-9, 2010.

Cooley, D., Nychka, D., and Naveau, P.: Bayesian spatial modeling of extreme precipitation return levels, Journal of the American Statistical Association, 102, 824–840, https://doi.org/10.1198/016214506000000780, 2007.

D'Agostino, R. B. and Stephens, M. A.: Goodness-of-Fit Techniques., Marcel Dekker, 1986.

De Cicco, L. A., Hirsch, R. M., Lorenz, D., and Watkins, W.: DataRetrieval: R packages for discovering and retrieving water data available from U.S. federal hydrologic web services, https://doi.org/10.5066/P9X4L3GE, 2018.

Enfield, D. B., Mestas-Nuñez, A. M., and Trimble, P. J.: The Atlantic Multidecadal Oscillation and its relation to rainfall and river flows in the continental U.S., Geophysical Research Letters, 28, 2077–2080, https://doi.org/10.1029/2000GL012745, 2001.

Gelman, A. and Hill, J.: Data Analysis Using Regression and Multilevel/Hierarchical Models, Cambridge University Press, Cambridge, https://doi.org/10.1017/CBO9780511790942, 2006.

Gelman, A. and Rubin, D. B.: Inference from iterative simulation using multiple sequences, Statistical Science, 7, 457–472, https://doi.org/10.1214/ss/1177011136, 1992.

Genest, C. and Favre, A.-C.: Everything You Always Wanted to Know about Copula Modeling but Were Afraid to Ask, Journal of Hydrologic Engineering, 12, 347–368, https://doi.org/10.1061/(asce)1084-0699(2007)12:4(347), 2007.

Ghile, Y. B. and Schulze, R. E.: Evaluation of three numerical weather prediction models for short and medium range agrohydrological applications, Water Resources Management, 24, 1005–1028, https://doi.org/10.1007/s11269-009-9483-5, 2010.

Gibbons, J. D. and Chakraborti, S.: Nonparametric Statistical Inference, Marcel Dekker, Inc., New York, NY, 4 edn., 1992.

Gneiting, T. and Raftery, A. E.: Strictly proper scoring rules, prediction, and estimation, Journal of the American Statistical Association, 102, 359–378, https://doi.org/10.1198/016214506000001437, 2007.

Gneiting, T., Stanberry, L. I., Grimit, E. P., Held, L., and Johnson, N. A.: Assessing probabilistic forecasts of multivariate quantities, with an application to ensemble predictions of surface winds, Test, 17, 211–235, https://doi.org/10.1007/s11749-008-0114-x, 2008.

Grantz, K., Rajagopalan, B., Clark, M., and Zagona, E.: A technique for incorporating large-scale climate information in basin-scale ensemble streamflow forecasts, Water Resources Research, 41, 10 410, https://doi.org/10.1029/2004WR003467, 2005.

He, J., Anderson, A., and Valeo, C.: Bias compensation in flood frequency analysis, Hydrological Sciences Journal, 60, 381–401, https://doi.org/10.1080/02626667.2014.885651, 2015.

Henze, N. and Zirkler, B.: A class of invariant consistent tests for multivariate normality, Communications in Statistics - Theory and Methods, 19, 3595–3617, https://doi.org/10.1080/03610929008830400, 1990.

Hersbach, H.: Decomposition of the continuous ranked probability score for ensemble prediction systems, Weather and Forecasting, 15, 559–570, https://doi.org/10.1175/1520-0434(2000)015<0559:DOTCRP>2.0.CO;2, 2000.

Hidalgo, H. G.: Climate precursors of multidecadal drought variability in the western United States, Water Resources Research, 40, 1–10, https://doi.org/10.1029/2004WR003350, 2004.

Hochrainer-Stigler, S.: Extreme and Systemic Risk Analysis, Integrated Disaster Risk Management, Springer Singapore, Singapore, integrated edn., https://doi.org/10.1007/978-981-15-2689-3, 2020.

Kahya, E. and Dracup, J. A.: The influences of Type 1 El Nino and La Nina events on streamflows in the Pacific southwest of the United States, Journal of Climate, 7, 965–976, https://doi.org/10.1175/1520-0442(1994)007<0965:TIOTEN>2.0.CO;2, 1994.

Katz, R. W.: Statistical Methods for Nonstationary Extremes, in: Extremes in a Changing Climate, edited by AghaKouchak, A., Easterling, D., Hsu, K., Schubert, S., and Sorooshian, S., pp. 15–37, Springer, Dordrecht, Dordrecht, 65 edn., https://doi.org/10.1007/978-94-007-4479-0_2, 2013.

Koster, R. D., Mahanama, S. P., Livneh, B., Lettenmaier, D. P., and Reichle, R. H.: Skill in streamflow forecasts derived from large-scale estimates of soil moisture and snow, Nature Geoscience, 3, 613–616, https://doi.org/10.1038/ngeo944, 2010.

Kurian, C., Sudheer, K. P., Vema, V. K., and Sahoo, D.: Effective flood forecasting at higher lead times through hybrid modelling framework, Journal of Hydrology, 587, https://doi.org/10.1016/j.jhydrol.2020.124945, 2020.

Kwon, H. H., Brown, C., Xu, K., and Lall, U.: Seasonal and annual maximum streamflow forecasting using climate information: Application to the Three Gorges Dam in the Yangtze River basin, China, Hydrological Sciences Journal, 54, 582–595, https://doi.org/10.1623/hysj.54.3.582, 2009.

Lima, C. H. and Lall, U.: Climate informed monthly streamflow forecasts for the Brazilian hydropower network using a periodic ridge regression model, Journal of Hydrology, 380, 438–449, https://doi.org/10.1016/j.jhydrol.2009.11.016, 2010.

Livneh, B. and Badger, A. M.: Drought less predictable under declining future snowpack, Nature Climate Change, 10, 452–458, https://doi.org/10.1038/s41558-020-0754-8, 2020.

Mardia, K. V.: Measures of Multivariate Skewness and Kurtosis with Applications, Biometrika, 57, 519, https://doi.org/10.2307/2334770, 1970.

McCabe, G. J. and Dettinger, M. D.: Decadal variations in the strength of ENSO teleconnections with precipitation in the western United States, International Journal of Climatology, 19, 1399–1410, https://doi.org/10.1002/(SICI)1097-0088(19991115)19:13<1399::AID-JOC457>3.0.CO;2-A, 1999.

McCabe, G. J., Clark, M. P., and Hay, L. E.: Rain-on-snow events in the western United States, Bulletin of the American Meteorological Society, 88, 319–328, https://doi.org/10.1175/BAMS-88-3-319, 2007.

Menne, M. J., Durre, I., Vose, R. S., Gleason, B. E., and Houston, T. G.: An Overview of the Global Historical Climatology Network-Daily Database, Journal of Atmospheric and Oceanic Technology, 29, 897–910, https://doi.org/10.1175/JTECH-D-11-00103.1, 2012.

Musselman, K. N., Lehner, F., Ikeda, K., Clark, M. P., Prein, A. F., Liu, C., Barlage, M., and Rasmussen, R.: Projected increases and shifts in rain-on-snow flood risk over western North America, https://doi.org/10.1038/s41558-018-0236-4, 2018.

Nowak, K., Hoerling, M., Rajagopalan, B., and Zagona, E.: Colorado river basin hydroclimatic variability, Journal of Climate, 25, 4389–4403, https://doi.org/10.1175/JCLI-D-11-00406.1, 2012.

Pagano, T. C.: Hydrology: soils,soils, snow and streamflow, https://doi.org/10.1038/ngeo948, 2010.

Pagano, T. C., Garen, D. C., Perkins, T. R., and Pasteris, P. A.: Daily Updating of Operational Statistical Seasonal Water Supply Forecasts for the western U.S., JAWRA Journal of the American Water Resources Association, 45, 767–778, https://doi.org/10.1111/j.1752-1688.2009.00321.x, 2009.

Penn, C. A., Clow, D. W., Sexstone, G. A., and Murphy, S. F.: Changes in Climate and Land Cover Affect Seasonal Streamflow Forecasts in the Rio Grande Headwaters, Journal of the American Water Resources Association, 56, 882–902, https://doi.org/10.1111/1752-1688.12863, 2020.

Plummer, M.: JAGS: A program for analysis of Bayesian graphical models using Gibbs sampling, 2003.

Plummer, M.: rjags: Bayesian graphical models using MCMC, 2019.

R Core, T.: R: A Language and Environment for Statistical Computing, 2017.

Rajagopalan, B., Cook, E., Lall, U., and Ray, B. K.: Spatiotemporal variability of ENSO and SST teleconnections to summer drought over the United States during the twentieth century, Journal of Climate, 13, 4244–4255, https://doi.org/10.1175/1520-0442(2000)013<4244:SVOEAS>2.0.CO;2, 2000.

Redmond, K. T. and Koch, R. W.: Surface Climate and Streamflow Variability in the Western United States and Their Relationship to Large-Scale Circulation Indices, Water Resources Research, 27, 2381–2399, https://doi.org/10.1029/91WR00690, 1991.

Regonda, S. K., Rajagopalan, B., Clark, M., and Zagona, E.: A multimodel ensemble forecast framework: Application to spring seasonal flows in the Gunnison River Basin, Water Resources Research, 42, 9404, https://doi.org/10.1029/2005WR004653, 2006.

Renard, B.: A Bayesian hierarchical approach to regional frequency analysis, Water Resources Research, 47, https://doi.org/10.1029/2010WR010089, 2011.

Robert, C. and Casella, G.: A short history of Markov Chain Monte Carlo: Subjective recollections from incomplete data, Statistical Science, 26, 102–115, https://doi.org/10.1214/10-STS351, 2011.

Robertson, D. E. and Wang, Q. J.: A Bayesian approach to predictor selection for seasonal streamflow forecasting, Journal of Hydrometeorology, 13, 155–171, https://doi.org/10.1175/JHM-D-10-05009.1, 2012.

Royston, J. P.: An Extension of Shapiro and Wilk's W Test for Normality to Large Samples, Applied Statistics, 31, 115, https://doi.org/10.2307/2347973, 1982.

Ruiz, J. E., Cordery, I., and Sharma, A.: Forecasting streamflows in Australia using the tropical Indo-Pacific thermocline as predictor, Journal of Hydrology, 341, 156–164, https://doi.org/10.1016/j.jhydrol.2007.04.021, 2007.

Safeeq, M., Shukla, S., Arismendi, I., Grant, G. E., Lewis, S. L., and Nolin, A.: Influence of winter season climate variability on snow–precipitation ratio in the western United States, International Journal of Climatology, 36, 3175–3190, https://doi.org/10.1002/JOC.4545, 2016.

Sankarasubramanian, A. and Lall, U.: Flood quantiles in a changing climate: Seasonal forecasts and causal relations, Water Resources Research, 39, https://doi.org/10.1029/2002WR001593, 2003.

Spiegelhalter, D. J., Best, N. G., Carlin, B. P., and van der Linde, A.: Bayesian measures of model complexity and fit, Journal of the Royal Statistical Society: Series B (Statistical Methodology), 64, 583–639, https://doi.org/10.1111/1467-9868.00353, 2002.

Thieken, A. H., Apel, H., and Merz, B.: Assessing the probability of large-scale flood loss events: a case study for the river Rhine, Germany, Journal of Flood Risk Management, 8, 247–262, https://doi.org/10.1111/JFR3.12091, 2015.

Thomson, A. M., Brown, R. A., Rosenberg, N. J., Izaurralde, R. C., Legler, D. M., and Srinivasan, R.: Simulated impacts of El Niño/Southern Oscillation on United States water resources, Journal of the American Water Resources Association, 39, 137–148, https://doi.org/10.1111/j.1752-1688.2003.tb01567.x, 2003.

Timilsena, J., Piechota, T., Tootle, G., and Singh, A.: Associations of interdecadal/interannual climate variability and long-term colorado river basin streamflow, Journal of Hydrology, 365, 289–301, https://doi.org/10.1016/j.jhydrol.2008.11.035, 2009.

Tootle, G. A., Piechota, T. C., and Singh, A.: Coupled oceanic-atmospheric variability and U.S. streamflow, Water Resources Research, 41, 1–11, https://doi.org/10.1029/2005WR004381, 2005.

Werner, K. and Yeager, K.: Challenges in forecasting the 2011 runoff season in the colorado basin, Journal of Hydrometeorology, 14, 1364–1371, https://doi.org/10.1175/JHM-D-12-055.1, 2013.

Werner, K., Brandon, D., Clark, M., and Gangopadhyay, S.: Climate Index Weighting Schemes for NWS ESP-Based Seasonal Volume Forecasts, Journal of Hydrometeorology, 5, 1076–1090, http://www.jstor.org/stable/24909975, 2004.

Wijayarathne, D. B. and Coulibaly, P.: Identification of hydrological models for operational flood forecasting in St. John's, Newfoundland, Canada, Journal of Hydrology: Regional Studies, 27, https://doi.org/10.1016/j.ejrh.2019.100646, 2020.

Wood, A. W., Hopson, T., Newman, A., Brekke, L., Arnold, J., and Clark, M.: Quantifying streamflow forecast skill elasticity to initial condition and climate prediction skill, Journal of Hydrometeorology, 17, 651–668, https://doi.org/10.1175/JHM-D-14-0213.1, 2016.